Plexcitonic quantum light emission from nanoparticle-on-mirror cavities

R. Sáez-Blázquez,[*,†,‡] A. Cuartero-González,[†,¶] J. Feist,[†] F. J. García-Vidal,[†,§] and A. I. Fernández-Domínguez[*,†]

†*Departamento de Física Teórica de la Materia Condensada and Condensed Matter Physics Center (IFIMAC), Universidad Autónoma de Madrid, 28049 Madrid, Spain*

‡*Vienna Center for Quantum Science and Technology, Atominstitut, TU Wien, 1040 Vienna, Austria*

¶*Mechanical Engineering Department, ICAI, Universidad Pontificia Comillas, 28015 Madrid, Spain*

§*Institute of High Performance Computing, Agency for Science, Technology, and Research (A*STAR), Singapore 138632, Singapore*

E-mail: rocio.saez.blazquez@tuwien.ac.at; a.fernandez-dominguez@uam.es

Abstract

We investigate the quantum-optical properties of the light emitted by a nanoparticle-on-mirror cavity filled with a single quantum emitter. Inspired by recent experiments, we model a dark-field set-up and explore the photon statistics of the scattered light under grazing laser illumination. Exploiting analytical solutions to Maxwell's equations, we quantize the nanophotonic cavity fields and describe the formation of plasmon-exciton polaritons (or plexcitons) in the system. This way, we reveal that the rich plasmonic spectrum of the nanocavity offers unexplored mechanisms for nonclassical light generation that are more efficient than the resonant interaction between the emitter

1

natural transition and the brightest optical mode. Specifically, we find three differ-
ent sample configurations in which strongly antibunched light is produced. Finally,
we illustrate the power of our approach by showing that the introduction of a second
emitter in the platform can enhance photon correlations further.

Keywords

plexciton, nanocavity, quantum emitter, antibunching, quantum light

Surface plasmons (SPs) have been largely exploited to tailor the classical (spatial and
temporal) characteristics of the electromagnetic (EM) fields produced by single molecules
and quantum dots[1,2]. Two paradigmatic examples of such manipulation are the reshaping
of their dipolar radiation pattern by directional nanoantennas[3,4] or the Purcell reduction of
their natural lifetime in nanogaps[5,6]. In recent years, this ability of SPs for EM control has
been also transferred into the quantum arena[7,8]. Initial efforts focused on the imprinting
of nonclassical features, such as entanglement[9], quadrature squeezing[10], or sub-Poissonian
statistics[11], in plasmonic waves through the incident, driving fields. In this context, quantum
emitters (QEs) were used as the optical sources that allowed the near-field launching of
confined single plasmons in metallic nanowires[12,13].

The quest for plasmon-assisted generation of radiative quantum states of light, propagat-
ing in free-space and into the far-field, has attracted much attention lately[14]. Devices based
on guiding geometries decorated with in- and out-coupling elements have been thoroughly
investigated [15,16]. SPs suffer heavily from metallic absorption in these extended systems.
For this reason, nanocavities have emerged as an alternative for nonclassical light sources of
smaller dimensions. Importantly, these nanostructures also make it possible to fully harness
the large density of photonic states associated with SPs[17]. Theoretical studies have shown
that the weak interaction between a single QE and a metallic nanosphere gives rise to mod-
erate photon antibunching and reduction of quantum-optical fluctuations[18–21]. Accordingly,
the measurement of second-order correlation functions below unity is taken as proof of the

2

single emitter operation in experiments on the Purcell effect in plasmonic antennas[22,23].

The realization of stronger quantum nonlinearities with larger near-to-far-field transfer efficiencies requires nanocavity-QE samples that function in the strong-coupling regime[24]. This leads to the formation of hybrid SP-QE states, usually termed as plexcitons[25–27], whose properties can be tuned through the admixture of the interactive character of excitons and the coherence and ubiquity of photons. This phenomenon does not only offer new avenues for light generation, but also lies at the core of the emergent field of polaritonic chemistry[28,29]. The accurate description of the signature of SP-QE interactions in far-field optical signals relies on the EM quantization in nanometer-sized, lossy structures, which is an area of intense activity at the moment[30–33]. Concurrently, plexciton formation in various QE-nanocavity platforms have been realized experimentally[34–38], and a number of theoretical models have investigated the emergence of photon correlations in these systems[39–42].

In this Letter, we investigate theoretically the quantum optical properties that plexciton strong coupling induces in the light scattered by a plasmonic cavity[43,44] in a dark-field set-up[45,46]. Through radiative-corrected quasi-static EM calculations[47,48], we describe the near-field and radiative characteristics of the SP modes sustained by the structure, as well as their interaction with a molecule placed at its gap. We characterize first the response of the bare cavity under grazing laser excitation. Secondly, we describe the far-field intensity and second-order correlation spectra for the configuration most explored experimentally[34,35,37]: QE at resonance with the brightest, dipolar (lowest in frequency) SP mode. We perform next a comprehensive study of the dependence of photon correlations on the detuning between QE and laser frequencies, as well as on the cavity gap size. Thus, we reveal three different parameter ranges in which strong antibunching can be attained. Finally, we illustrate the power of our approach by introducing a second QE in the system. We find that the second-order correlation function can be further reduced this way[49], thanks to the emergence of new pathways for destructive quantum interference in the plexciton ladder.

Theoretical Modelling

[Figure 1](a) sketches the system of interest: an archetypal nanoparticle-on-mirror (NPoM) cavity, formed by a $D = 30$ nm diameter nanosphere separated by a few-nanometer gap from a planar substrate[34,44]. Both are metallic, with permittivity given by a Drude fitting for silver, $\epsilon(\omega) = \epsilon_\infty - \omega_\mathrm{p}^2/\omega(\omega + \mathrm{i}\gamma_\mathrm{m})$, where $\hbar\omega_\mathrm{p} = 8.91$ eV, $\epsilon_\infty = 9.7$ and $\hbar\gamma_\mathrm{m} = 0.06$ eV. For simplicity, the background refractive index is set to unity. We employ an analytical, two-dimensional model that we recently developed (see Ref.[48] for more details) to describe the SP modes sustained by this geometry (fully defined by the diameter D and gap size δ). This tool is based on quasi-static solutions to Maxwell's equations and is refined by means of the so-called radiative-reaction correction[50,51], yielding an excellent agreement with numerical EM simulations. A QE is placed in the NPoM gap. It is characterized by its transition dipole moment, μ_E, transition frequency, ω_E, radiative, γ_rad, and non-radiative, γ_nrad, decay rates, as well as its dephasing rate, γ_deph. Note that the QE radiative decay rate is simply $\gamma_\mathrm{rad} = \omega_\mathrm{E}^3\mu_\mathrm{E}^2/(3\pi\epsilon_0\hbar c^3)$[52] (where ϵ_0 is the vacuum permittivity and c the speed of light) and its nonradiative decay is set by its intrinsic quantum yield $\mathrm{QY} = \gamma_\mathrm{rad}/(\gamma_\mathrm{rad} + \gamma_\mathrm{nrad})$. The hybrid NPoM-QE sample is driven by a grazing laser field of frequency ω_L and amplitude E_L, mimicking a dark-field-like illumination.

Our quasi-static treatment allows the labelling of the NPoM modes in terms of two quantum numbers, their azimuthal order, $n = 1, 2, 3\ldots$, and the odd/even parity of their associated EM fields across the gap center, $\sigma = \pm 1$[51]. Here, to simplify the notation, we combine both in a single index $\alpha = \{n, \sigma\}$. Our theory also yields their natural frequencies, ω_α, and broadening, $\gamma_\alpha = \gamma_\mathrm{m} + \gamma_\alpha^\mathrm{rad}$. Note that plasmonic absorption is the same for all SPs, given by the Drude damping, and their radiative decay is proportional to the square of their dipole moment, $\gamma_\alpha^\mathrm{rad} \propto \mu_\alpha^2$, but the usual free-space expression has to be corrected by the image charge distribution induced in the metal substrate[48]. We also obtained closed expressions for the QE-SP coupling strengths, g_α, and their dependence on the QE parameters (position and natural frequency).

In the rotating frame[53], set by the laser frequency ω_L, and under the rotating-wave approximation[54], the Hamiltonian for the set-up in Figure 1(a) is[49]

$$
\begin{aligned}
\hat{H} &= \hbar(\omega_\text{E} - \omega_\text{L})\hat{\sigma}^\dagger\hat{\sigma} + \sum_\alpha \hbar(\omega_\alpha - \omega_\text{L})\hat{a}_\alpha^\dagger\hat{a}_\alpha + \\
&+ \sum_\alpha \hbar g_\alpha(\hat{\sigma}^\dagger\hat{a}_\alpha + \hat{\sigma}\hat{a}_\alpha^\dagger) + \hbar\Omega_\text{E}(\hat{\sigma}^\dagger + \hat{\sigma}) + \\
&+ \sum_\alpha \hbar\Omega_\alpha(\hat{a}_\alpha^\dagger + \hat{a}_\alpha),
\end{aligned} \tag{1}
$$

where $\hat{a}_\alpha$ and $\hat{\sigma}$ are the SP and QE annihilation operators, respectively. Note that the third term in Equation 1 describes the light-matter coupling, where $\hbar g_\alpha = \mathbf{E}_\alpha^{(1)} \cdot \boldsymbol{\mu}_\text{E}$ and $\mathbf{E}_\alpha^{(1)}$ is the quantized one-photon field strength of mode α at the QE position. Then, $\hbar\Omega_\text{E} = \boldsymbol{E}_\text{L} \cdot \boldsymbol{\mu}_\text{E}$ and $\hbar\Omega_\alpha = \boldsymbol{E}_\text{L} \cdot \boldsymbol{\mu}_\alpha$ are the coherent pumping amplitudes. Note that dipole moments and incident fields are oriented vertically in Figure 1(a). The master equation for the steady-state of the system including SP damping and QE decay and dephasing reads

$$
\begin{aligned}
&\frac{\text{i}}{\hbar}[\hat{\rho}, \hat{H}] + \sum_\alpha \frac{\gamma_\alpha}{2}\mathcal{L}_{\hat{a}_\alpha}[\hat{\rho}] + \\
&+ \frac{\gamma_\text{rad} + \gamma_\text{nrad}}{2}\mathcal{L}_{\hat{\sigma}}[\hat{\rho}] + \frac{\gamma_\text{deph}}{2}\mathcal{L}_{\hat{\sigma}^\dagger\hat{\sigma}}[\hat{\rho}] = 0,
\end{aligned} \tag{2}
$$

where the Lindblad terms have the usual form $\mathcal{L}_{\hat{\mathcal{O}}} = 2\hat{\mathcal{O}}\hat{\rho}\hat{\mathcal{O}}^\dagger - \hat{\mathcal{O}}^\dagger\hat{\mathcal{O}}\hat{\rho} - \hat{\rho}\hat{\mathcal{O}}^\dagger\hat{\mathcal{O}}$.

Results and discussion

Before investigating far-field optical signatures of light-matter interactions in the hybrid QE-SP system, we employ our theory to characterize the bare plasmonic cavity first. We compute the spectral density weighting the local density of photonic states and the QE-SP

coupling strength at the NPoM gap. We have recently shown that this is given by[33]

$$
\begin{aligned}
J(\omega) &= \frac{\hbar}{\pi} \mathrm{Im} \left\{ \sum_{\alpha} g_{\alpha} \left(\tilde{\mathbf{H}} - \hbar\omega \right)^{-1}_{\alpha\alpha} g_{\alpha} \right\} \\
&= \sum_{\alpha} \frac{g_{\alpha}^2}{\pi} \frac{\gamma_{\alpha}/2}{(\omega - \omega_{n,\sigma})^2 + \gamma_{\alpha}^2/4},
\end{aligned} \tag{3}
$$

where $\tilde{\mathbf{H}}_{\alpha\beta} = \hbar \left(\omega_{\alpha} - \mathrm{i}\frac{\gamma_{\alpha}}{2} \right) \delta_{\alpha\beta}$ is equal to the coefficient matrix of the SP modes in the effective non-Hermitian Hamiltonian governing the coherent evolution in the Lindblad master equation.

Figure 1 (b) renders the spectral density at the center of the NPoM gap, $z_{\mathrm{E}} = 0.5\,\delta$ ($z = 0$ corresponds to the substrate surface), for cavities with $D = 30\,\mathrm{nm}$ and δ ranging from 0.9 (purple) to 5.4 nm (light green). The coupling constants are proportional to the QE dipole moment, $\mathrm{g}_{\alpha} \propto \mu_{\mathrm{E}}$. They were evaluated at $\mu_{\mathrm{E}} = 0.55$ e·nm, the value which we will consider in our plexcitonic systems. As previously reported[27], the smaller the gap, the larger $J(\omega)$. In all cases, the spectra present a low-frequency maximum originating from the brightest, dipolar SP mode, $\alpha = \{1,1\}$, which redshifts with decreasing δ; and another maximum in the vicinity of the asymptotic surface plasmon frequency ($\omega_{\mathrm{P}}/\sqrt{1 + \epsilon_{\infty}}$) due to the pseudomode that results from the spectral overlapping of high order SPs[55]. For small enough gap sizes, the contributions from quadrupolar and higher order even modes (specifically, $\alpha = \{2-4, 1\}$) are also apparent.

We focus next on the far-field response of the bare NPoM structure. We compute the scattering spectrum by solving Equation 2 removing all the QE-related terms. Once the SP steady-state density matrix, $\hat{\rho}_{\mathrm{SP}}$, is known, the far-field scattering intensity can be computed as

$$
I_{\mathrm{SP}} = \langle \hat{E}_{\mathrm{SP}}^- \hat{E}_{\mathrm{SP}}^+ \rangle = \sum_{\alpha,\beta} \mu_{\alpha}\mu_{\beta}\mathrm{tr}\{\hat{a}_{\alpha}^{\dagger}\hat{a}_{\beta}\hat{\rho}_{\mathrm{SP}}\}, \tag{4}
$$

where $\hat{E}_{\mathrm{SP}}^- = \sum_{\alpha} \mu_{\alpha}\hat{a}_{\alpha}^{\dagger}$ is the (negative frequency part of the) electric far-field operator. For simplicity, we are dropping the Dyadic Green's function in the definition of the electric

field operator, which would account for the spatial pattern of the cavity fields. Importantly, the cross terms in Equation 1 reflect the emergence of superposition effects in the photon emission from different SP modes.

Figure 1(c) plots the scattering spectra for the NPoM configurations in Figure 1(b). Dash-dotted lines correspond to COMSOL Multiphysics$^{\text{TM}}$ simulations of the scattering efficiency (defined as the cross section normalized to physical size) in the quasi-static limit, while solid lines plot the prediction from Equation 4. Note that the latter have been scaled vertically (by the same factor for all δ) to facilitate the comparison between both sets of data. We can observe that the spectra are governed by a large peak at laser frequencies in the vicinity of the lowest, dipolar SP ($\alpha = \{1, 1\}$). The condition $\omega_{\text{L}} = \omega_{\text{dip}}$ is indicated by vertical dotted lines in all cases. Higher order SP maxima are also evident, specially at small δ. On the contrary, there is not any pseudomode signature in the scattering signal, as expected from the dark character of the SP modes that form it. The NPoM spectra in Figure 1(c) present scattering minima at laser frequencies between SP resonances. These are the so-called invisibility dips, which emerge (more clearly in log scale) due to the destructive interference in the photon emission by different plasmonic channels[51].

Next, we place a vertically-oriented QE at the center of the gap of the NPoM geometries in Figure 1. Reproducing previous experimental setups, we set the QE frequency at resonance with the dipolar SP, $\omega_{\text{E}} = \omega_{\text{dip}}$, which is different for each δ. This way, the signature of QE-SP interaction is expected to be most apparent in the far-field. We take QY=0.65, in agreement with values reported for molecular dyes, such as Atto 647N[38]. The associated radiative and nonradiative decay rates are therefore in the $10^{-6} - 10^{-7}$ eV range (note that these depend on ω_{E}). Additionally, we consider a QE dephasing rate of $\gamma_{\text{deph}} = 1$ meV[56]. The spectra for the hybrid NPoM-QE system can be obtained from the steady-state density matrix solution, $\hat{\rho}$, for the full master equation in Equation 2,

$$I_{\text{scat}} = \langle \hat{E}_{\text{scat}}^{-} \hat{E}_{\text{scat}}^{+} \rangle = \text{tr}\{\hat{E}_{\text{scat}}^{-} \hat{E}_{\text{scat}}^{+} \hat{\rho}\}, \tag{5}$$

where in order to account for the open character of the plasmonic cavity, the electric field operator, $\hat{E}_{\text{scat}}^- = \hat{E}_{\text{SP}}^- + \mu_{\text{E}}\hat{\sigma}^\dagger$, includes now the emission from the molecule itself[49]. Note that we can also compute the density matrix, $\hat{\rho}_{\text{E}}$, and scattering intensity for the free-standing emitter, obtained from the QE terms in Equation 2 and $I_{\text{E}} = \mu_{\text{E}}^2 \text{tr}\{\hat{\sigma}^\dagger \hat{\sigma} \hat{\rho}_{\text{E}}\}$.

Figure 2(a) shows the scattering intensity versus $\hbar(\omega_{\text{L}} - \omega_{\text{dip}})$, the laser detuning with respect to the dipolar SP, which allows the direct comparison between different cavities. Dashed lines correspond to the Lorentzian-like spectral profile of I_{SP} for all structures, while solid lines plot the spectra for the plexcitonic samples. For reference, the red dotted line shows I_{E} normalized to the nanoparticle size, whose linewidth is given by $\gamma_{\text{E}} = \gamma_{\text{rad}} + \gamma_{\text{nrad}} + \gamma_{\text{deph}} \simeq 1$ meV. For large gaps, and therefore lower QE-SP coupling strengths, the presence of the molecule leads to the appearance of a scattering dip at $\omega_{\text{L}} = \omega_{\text{E}}$ of width similar to γ_{E}. This phenomenology, closely related to the electromagnetic induced transparency, is in accordance with that reported previously for single metallic nanoparticles in the weak-interaction regime[19]. For small δ, the far-field spectra develop a well-defined Rabi doublet lineshape. This is the fingerprint of the onset of strong coupling between the bright plasmon mode and the molecule[34]. These two scattering maxima are originated from the upper and lower plexcitonic states that have been formed in the cavity (see below). Two different mechanisms contribute to make the intensity of the lower plexciton larger than the upper one. On the one hand, the former (latter) results from the constructive (destructive) interference of the SP and QE emission channels[49]. On the other hand, it has been shown that, despite being highly detuned, higher frequency, neighboring SP modes can also increase the Rabi asymmetry in these systems[48].

Our approach enables us to characterize the light scattered by the NPoM-QE system beyond the intensity spectra above. We can employ it to analyze the scattered photon statistics through the so-called zero-delay second-order correlation function[54]

$$g^{(2)}(0) = \langle \hat{E}_{\text{scat}}^- \hat{E}_{\text{scat}}^- \hat{E}_{\text{scat}}^+ \hat{E}_{\text{scat}}^+ \rangle / I_{\text{scat}}^2 \ , \tag{6}$$

8

which gives the probability of detecting two coincident photons in the far-field. Although not discussed above, the bosonic character of SPs yields $g^{(2)}(0) = 1$ for the bare NPoM cavities in Figure 1. In the following, we will explore the conditions in which the plexcitonic system deviates from these Poissonian statistics, with special focus on the emergence of negative correlations, antibunching or sub-Poissonian statistics. With all these terms we will refer to photon emission characterized by a second-order correlation function below unity, $g^{(2)}(0) < 1$.

In Figure 2(b), we plot the zero-delay second-order correlation function for the NPoM-QE samples in panel (a). Vertical dotted lines indicate the two plexciton frequencies in the first manifold for all geometries (which coincide with the scattering intensity maxima[39]). We can observe that $g^{(2)}(0) \gg 1$, bunched emission or more rigorously, super-Poissonian statistics, takes place between them. The maximum in $g^{(2)}(0)$ occurs at $\omega_L \simeq \omega_E$ and redshifts and increases with decreasing gap size (larger QE-SP coupling). Only for $\delta = 0.9$ nm (purple line) negative photon correlations are apparent. A region of moderate antibunching, $g^{(2)}(0) > 0.8$, develops for laser frequencies slightly below the lower plexciton frequency (note that an even shallower dip also occurs at ω_L above the upper plexciton). The correlation spectra overlap with those obtained by neglecting photon emission by SP modes different from the dipolar one, which therefore do not play any role in this particular NPoM-QE configuration.

The negative correlations observed in Figure 2(b) can be attributed to the so-called *photon blockade effect*[57,58], where the presence of an excitation in the system prevents the absorption of a second photon of the same frequency due to the anharmonicity of the plexciton ladder. This phenomenon becomes stronger as the light-matter interaction strengthens, which means that smaller gap sizes or larger QE dipole moments would be required to reduce $g^{(2)}(0)$ further. However, there exists another effect yielding sub-Poissonian photon emission, known as interference-induced or *unconventional antibunching*[59,60]. Thoroughly analyzed in single-mode semiconductor microcavities[61], it develops only when the driving laser is far from resonance, and due to destructive quantum interference among different de-excitation

9

pathways in the system. In the following, we investigate the emergence of both antibunching mechanisms in our plexcitonic samples, exploring the full richness of the NPoM spectrum through the emitter and laser frequencies and the emitter position.

Figure 3 shows intensity (left panels) and second-order correlation function (central panels) maps as a function of the detuning of the laser with respect to the QE frequency (horizontal axes) and the emitter frequency itself (vertical axes). The gap size is fixed to $\delta = 0.9$ nm, and two different emitter positions are considered: at the center of the gap, $z_{\mathrm{E}} = 0.5\delta$ (top, a-c), and displaced vertically towards the nanoparticle surface, $z_{\mathrm{E}} = 0.85\delta$ (bottom, d-f). In these panels, the SP frequencies, $\hbar\omega_{\alpha}$, are marked by horizontal dotted lines. Note that the purple solid lines in Figure 2 correspond to horizontal cuts of Figure 3(a) and (b) in the vicinity of the dipolar SP. In this range of QE frequencies and below it ($\omega_{\mathrm{E}} \lesssim \omega_{\mathrm{dip}} = 2.26$ eV), I_{scat} develops a clear Rabi doublet lineshape, associated with the two plexcitons that emerge from the strong coupling of QE and dipolar SP. For red-detuned QEs, the lower (upper) plexciton has a more emitter-like (plasmon-like) character, and its position approaches ω_{E} (ω_{dip}). On the contrary, for blue detuned QEs, the signature of higher order SPs becomes apparent, and I_{scat} reproduces a similar anticrossing phenomenology as that around the dipolar SP mode. The intensity maps for both emitter positions are similar, with a remarkable difference: while the scattering dip between upper and lower plexcitons is always at $\omega_{\mathrm{L}} = \omega_{\mathrm{E}}$ at the gap center (a), it redshifts with increasing QE frequency for $z_{\mathrm{E}} = 0.85\delta$ (d). This is a direct consequence of the large coupling to the plasmonic pseudomode that the emitter experiences when it is placed in close proximity to the nanoparticle boundary. This is evident in the far-field spectra even for ω_{E} significantly detuned from the pseudomode frequency [48].

The photon correlation maps in Figure 3(b) and (d) show that $g^{(2)}(0)$ has a higher sensitivity on the QE position than I_{scat}. Both panels expose that bunching emission (yellow, $g^{(2)}(0) > 1$) takes place at the conditions for plexciton anticrossing, where I_{scat} is minimum. They also reveal that much stronger negative correlations than the resonant ($\omega_{\mathrm{E}} = \omega_{\mathrm{dip}}$)

10

configuration considered in Figure 2 can be achieved by exploiting the full plasmonic spectrum of NPoM cavities. To clarify the degree of antibunching attainable in these systems, Figure 3(c) and (f) plot the spectral minimum of $g^{(2)}(0)$ as a function of the QE frequency. For both z_E, a region of sub-Poissonian statistics is apparent at emitter frequencies below the dipolar SP, which becomes stronger and spectrally broader for lower ω_E. As we discussed above, at laser frequencies slightly below the emitter frequency, these negative correlations are generated via the photon blockade effect, yielding $g^{(2)}(0)$ values below 0.2. On the contrary, a weaker interference-induced antibunching takes place in this region but for $\omega_L > \omega_E$, see panels (b) and (e).

Another region yielding $g^{(2)}(0) < 1$ in Figure 3(b) and (e) occurs at QE frequencies approaching the pseudomode. Negative correlations are weaker than below the dipolar SP and, as discussed below, they have a different, interference-induced, origin. Note that these become more apparent for $z_E = 0.85\delta$, since the coupling to the higher-energy plasmon modes increases this way[27]. Antibunching also takes place in a third NPoM-QE configuration, at QE frequencies in between the dipolar (lowest) and the quadrupolar (second lowest, $\alpha = \{2, 1\}$) SP cavity modes ($2.3\,\mathrm{eV} \lesssim \hbar\omega_E \lesssim 2.5\,\mathrm{eV}$)—exactly at the parameter range where a scattering (invisibility) dip, due to destructive interference effects in the emission by these two SPs, evolves in I_{scat}[51]. We can therefore conclude that this phenomenon does not only emerge in the intensity spectrum, but also in the photon statistics. The QE position weights the relative coupling between the emitter and both cavity modes, and thus the strength of the interference that suppresses two-photon processes, which seems to be larger (reaching $g^{(2)}(0)$ below 0.2) for displaced emitters.

Lastly, we investigate whether, as previously reported for single-mode cavity models[39], the presence of a second emitter may be beneficial for the generation of nonclassical light in QE-SP systems. We consider two vertically-oriented emitters hosted in the small gap cavity above ($\delta = 0.9$ nm, $D = 30$ nm). The two QE positions are chosen to be the same as in Figure 3: $z_E = 0.50\delta$ and $z_E = 0.85\delta$. Figure 4 plots the second-order correlation function

versus the laser frequency for two different configurations, chosen from the single-emitter samples that yield sub-Poissonian emission in the same figure. In panel (a), both emitters are red-detuned with respect to the dipolar SP, while they are at the invisibility dip between the dipolar and quadrupolar modes in panel (b). Continuous lines plot $g^{(2)}(0)$ for the two emitters, while dashed lines represent the associated single-emitter cases. In both panels, we consider QE frequencies slightly separated, $\hbar(\omega_{E2} - \omega_{E1}) = 0.1$ eV, which is of the order of the Drude damping, γ_m. The correlation function for further QE-QE detunings is basically the superposition of the two single-emitter calculations. On the other hand, if ω_E is the same for both emitters, the plexciton emission is that of the single QE with a larger transition dipole moment. Figure 4 explores the intermediate regime: a significant enhancement of negative correlations is not apparent at low QE frequencies (a), but a strong reduction in $g^{(2)}(0)$ takes place for ω_{E1} and ω_{E2} at the invisibility dip. In particular, we observe a dip in the correlation function at laser frequencies between the two QE lines. In that minimum, $g^{(2)}(0) \sim 0.3$, while the corresponding single-emitter spectra do not present values below 0.7. Thus, we can conclude that indeed the interplay and interaction between various SP modes and QEs can be exploited to enhance the degree of antibunching in the photon emission by NPoM plexcitonic systems.

Conclusion

We have presented a master equation description of the far-field photon emission by a plasmonic nanoparticle-on-mirror cavity strongly coupled to a single molecule or quantum emitter. Parameterized through classical electromagnetic calculations, we have employed our model to characterize the classical and quantum optical properties of the light scattered by this hybrid system in a dark-field-like set-up. First, we have found that the formation of plexcitons does not yield significant antibunching in the most explored sample configuration, in which the molecular transition is at resonance with the dipolar cavity mode. Next, by

varying the laser and emitter frequencies, we have explored the whole plasmonic spectrum of the nanostructure. This way, we have found that large negative photon correlations take place at three different emitter frequencies: below the dipolar plasmon, at the invisibility dip between this mode and the quadrupolar one, and at resonance with the plasmonic pseudo-mode. Finally, we have demonstrated that, under certain conditions, photon antibunching can be enhanced through the introduction of a second molecule in the nanocavity. We believe that our theoretical findings shed light into recent experiments, and can serve as a guide for the design of devices for quantum light generation through the strong coupling of light and material states at the nanoscale.

Acknowledgment

References

(1) Giannini, V.; Fernández-Domínguez, A. I.; Heck, S. C.; Maier, S. A. *Chemical Reviews* **2011**, *111*, 3888–3912.

(2) Novotny, L.; Van Hulst, N. *Nature Photonics* **2011**, *5*, 83–90.

(3) Taminiau, T.; Stefani, F.; Segerink, F. B.; Van Hulst, N. *Nature Photonics* **2008**, *2*, 234–237.

(4) Curto, A. G.; Volpe, G.; Taminiau, T. H.; Kreuzer, M. P.; Quidant, R.; van Hulst, N. F. *Science* **2010**, *329*, 930–933.

(5) Farahani, J. N.; Pohl, D. W.; Eisler, H.-J.; Hecht, B. *Phys. Rev. Lett.* **2005**, *95*, 017402.

(6) Anger, P.; Bharadwaj, P.; Novotny, L. *Phys. Rev. Lett.* **2006**, *96*, 113002.

(7) Tame, M. S.; McEnery, K.; Özdemir, Ş.; Lee, J.; Maier, S. A.; Kim, M. *Nature Physics* **2013**, *9*, 329–340.

(8) Marquier, F.; Sauvan, C.; Greffet, J.-J. *ACS Photonics* **2017**, *4*, 2091–2101.

(9) Moreno, E.; García-Vidal, F. J.; Erni, D.; Cirac, J. I.; Martín-Moreno, L. *Phys. Rev. Lett.* **2004**, *92*, 236801.

(10) Huck, A.; Smolka, S.; Lodahl, P.; Sørensen, A. S.; Boltasseva, A.; Janousek, J.; Andersen, U. L. *Phys. Rev. Lett.* **2009**, *102*, 246802.

(11) Di Martino, G.; Sonnefraud, Y.; Kéna-Cohen, S.; Tame, M.; Özdemir, a. K.; Kim, M. S.; Maier, S. A. *Nano Letters* **2012**, *12*, 2504–2508.

(12) Chang, D. E.; Sorensen, A. S.; Hemmer, P. R.; Lukin, M. D. *Phys. Rev. Lett.* **2006**, *97*, 053002.

(13) Akimov, A.; Mukherjee, A.; Yu, C.; Chang, D.; Zibrov, A.; Hemmer, P.; Park, H.; Lukin, M. *Nature* **2007**, *450*, 402–406.

(14) A. I. Fernández-Domínguez, S. B.; Mortensen, N. A. *Acs Photonics* **2018**, *5*, 3447–3451.

(15) others,, et al. *Nature communications* **2015**, *6*, 1–9.

(16) Kumar, S.; Bozhevolnyi, S. I. *Advanced Quantum Technologies* **2021**, *4*, 2100057.

(17) Baumberg, J. J.; Aizpurua, J.; Mikkelsen, M. H.; Smith, D. R. *Nature materials* **2019**, *18*, 668–678.

(18) Waks, E.; Sridharan, D. *Phys. Rev. A* **2010**, *82*, 043845.

(19) Ridolfo, A.; Di Stefano, O.; Fina, N.; Saija, R.; Savasta, S. *Phys. Rev. Lett.* **2010**, *105*, 263601.

(20) Martín-Cano, D.; Haakh, H. R.; Murr, K.; Agio, M. *Phys. Rev. Lett.* **2014**, *113*, 263605.

(21) I. Liberal, I. E.; Ziolkowski, R. W. *Phys. Rev. A* **2018**, *97*, 053847.

(22) Hoang, T. B.; Akselrod, G. M.; Mikkelsen, M. H. *Nano Letters* **2016**, *16*, 270–275.

(23) Singh, A.; de Roque, P. M.; Calbris, G.; Hugall, J. T.; van Hulst, N. F. *Nano Letters* **2018**, *18*, 2538–2544.

(24) Törmä, P.; Barnes, W. L. *Reports on Progress in Physics* **2014**, *78*, 013901.

(25) Manjavacas, A.; García de Abajo, F. J.; Nordlander, P. *Nano Letters* **2011**, *11*, 2318–2323.

(26) Esteban, R.; Aizpurua, J.; Bryant, G. W. *New Journal of Physics* **2014**, *16*, 013052.

(27) Li, R.-Q.; Hernángomez-Pérez, D.; García-Vidal, F.; Fernández-Domínguez, A. *Phys. Rev. Lett.* **2016**, *117*, 107401.

(28) Feist, J.; Galego, J.; Garcia-Vidal, F. J. *ACS Photonics* **2018**, *5*, 205–216.

(29) Garcia-Vidal, F. J.; Ciuti, C.; Ebbesen, T. W. *Science* **2021**, *373*, eabd0336.

(30) Lalanne, P.; Yan, W.; Vynck, K.; Sauvan, C.; Hugonin, J.-P. *Laser & Photonics Reviews* **2018**, *12*, 1700113.

(31) Franke, S.; Hughes, S.; Dezfouli, M. K.; Kristensen, P. T.; Busch, K.; Knorr, A.; Richter, M. *Phys. Rev. Lett.* **2019**, *122*, 213901.

(32) Tserkezis, C.; Fernández-Domínguez, A. I.; Gonçalves, P.; Todisco, F.; Cox, J. D.; Busch, K.; Stenger, N.; Bozhevolnyi, S. I.; Mortensen, N. A.; Wolff, C. *Reports on Progress in Physics* **2020**, *83*, 082401.

(33) Medina, I.; García-Vidal, F. J.; Fernández-Domínguez, A. I.; Feist, J. *Phys. Rev. Lett.* **2021**, *126*, 093601.

(34) Chikkaraddy, R.; De Nijs, B.; Benz, F.; Barrow, S. J.; Scherman, O. A.; Rosta, E.; Demetriadou, A.; Fox, P.; Hess, O.; Baumberg, J. J. *Nature* **2016**, *535*, 127–130.

(35) Santhosh, K.; Bitton, O.; Chuntonov, L.; Haran, G. *Nature communications* **2016**, *7*, 1–5.

(36) Groß, H.; Hamm, J. M.; Tufarelli, T.; Hess, O.; Hecht, B. *Science advances* **2018**, *4*, eaar4906.

(37) Leng, H.; Szychowski, B.; Daniel, M.-C.; Pelton, M. *Nature communications* **2018**, *9*, 1–7.

(38) Ojambati, O. S.; Chikkaraddy, R.; Deacon, W. D.; Horton, M.; Kos, D.; Turek, V. A.; Keyser, U. F.; Baumberg, J. J. *Nature communications* **2019**, *10*, 1–7.

(39) Sáez-Blázquez, R.; Feist, J.; Fernández-Domínguez, A. I.; García-Vidal, F. J. *Optica* **2017**, *4*, 1363–1367.

(40) Peyskens, F.; Englund, D. *Phys. Rev. A* **2018**, *97*, 063844.

(41) Rousseaux, B.; Baranov, D. G.; Antosiewicz, T. J.; Shegai, T.; Johansson, G. *Phys. Rev. Research* **2020**, *2*, 033056.

(42) You, J.-B.; Xiong, X.; Bai, P.; Zhou, Z.-K.; Ma, R.-M.; Yang, W.-L.; Lu, Y.-K.; Xiao, Y.-F.; Png, C. E.; Garcia-Vidal, F. J.; Qiu, C.-W.; Wu, L. *Nano Letters* **2020**, *20*, 4645–4652.

(43) Tserkezis, C.; Esteban, R.; Sigle, D. O.; Mertens, J.; Herrmann, L. O.; Baumberg, J. J.; Aizpurua, J. *Physical Review A* **2015**, *92*, 053811.

(44) Li, G.-C.; Zhang, Q.; Maier, S. A.; Lei, D. *Nanophotonics* **2018**, *7*, 1865–1889.

(45) Knight, M. W.; Fan, J.; Capasso, F.; Halas, N. J. *Optics express* **2010**, *18*, 2579–2587.

(46) Lei, D. Y.; Fernández-Domínguez, A. I.; Sonnefraud, Y.; Appavoo, K.; Haglund, R. F.; Pendry, J. B.; Maier, S. A. *ACS Nano* **2012**, *6*, 1380–1386.

(47) Cuartero-González, A.; Fernández-Domínguez, A. I. *ACS Photonics* **2018**, *5*, 3415–3420.

(48) Cuartero-González, A.; Fernández-Domínguez, A. I. *Phys. Rev. B* **2020**, *101*, 035403.

(49) Sáez-Blázquez, R.; Feist, J.; García-Vidal, F. J.; Fernández-Domínguez, A. I. *Phys. Rev. A* **2018**, *98*, 013839.

(50) Carminati, R.; Greffet, J.-J.; Henkel, C.; Vigoureux, J. *Optics Communications* **2006**, *261*, 368–375.

(51) Aubry, A.; Lei, D. Y.; Maier, S. A.; Pendry, J. B. *ACS Nano* **2011**, *5*, 3293–3308.

(52) Novotny, L.; Hecht, B. *Principles of Nano-Optics*, 2nd ed.; Cambridge University Press, 2012.

(53) Gardiner, S. A. Theory and Application of Dark States in Cavity QED. Master's thesis, University of Waikato, 1995.

(54) Loudon, R. *The Quantum Theory of Light*, 3rd ed.; Oxford University Press, 2000.

(55) Delga, A.; Feist, J.; Bravo-Abad, J.; Garcia-Vidal, F. *Physical Review Letters* **2014**, *112*, 253601.

(56) Clear, C.; Schofield, R. C.; Major, K. D.; Iles-Smith, J.; Clark, A. S.; McCutcheon, D. P. S. *Phys. Rev. Lett.* **2020**, *124*, 153602.

(57) Imamoḡlu, A.; Schmidt, H.; Woods, G.; Deutsch, M. *Phys. Rev. Lett.* **1997**, *79*, 1467–1470.

(58) Birnbaum, K. M.; Boca, A.; Miller, R.; Boozer, A. D.; Northup, T. E.; Kimble, H. J. *Nature* **2005**, *436*, 87–90.

(59) Carmichael, H.; Brecha, R.; Rice, P. *Optics Communications* **1991**, *82*, 73–79.

(60) Rempe, G.; Thompson, R. J.; Brecha, R. J.; Lee, W. D.; Kimble, H. J. *Phys. Rev. Lett.* **1991**, *67*, 1727–1730.

(61) Radulaski, M.; Fischer, K. A.; Lagoudakis, K. G.; Zhang, J. L.; Vučković, J. *Phys. Rev. A* **2017**, *96*, 011801.
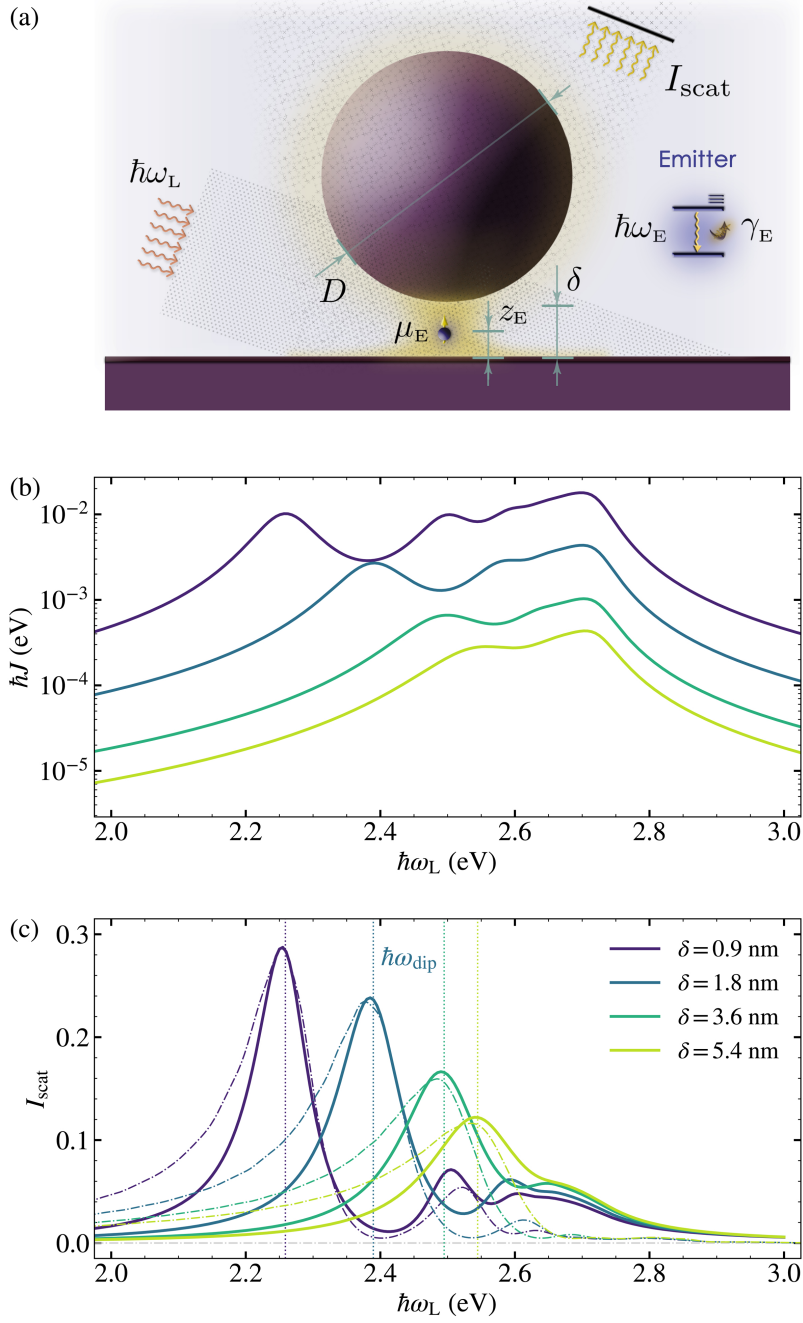
Graphical TOC Entry
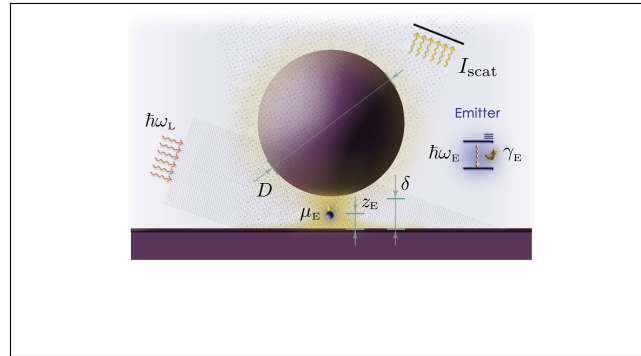
Figure 1: (a) Sketch of the system, composed of a single QE coupled to the SP fields within the gap of a NPoM cavity in a dark-field-like set-up. The inset shows the two-level scheme modelling the emitter. (b) Spectral density $J(\omega)$ at the gap center for different values of the gap size δ (with $D = 30$ nm). (c) Normalized dark-field scattering spectra for the bare cavities above. Solid lines represent I_{SP} given by Equation 4, while dash-dotted lines correspond to scattered intensity obtained by numerical EM calculations. Vertical dotted lines indicate the position of the lowest-order (dipolar) plasmon mode, with energy $\hbar\omega_{dip}$ for each gap size.
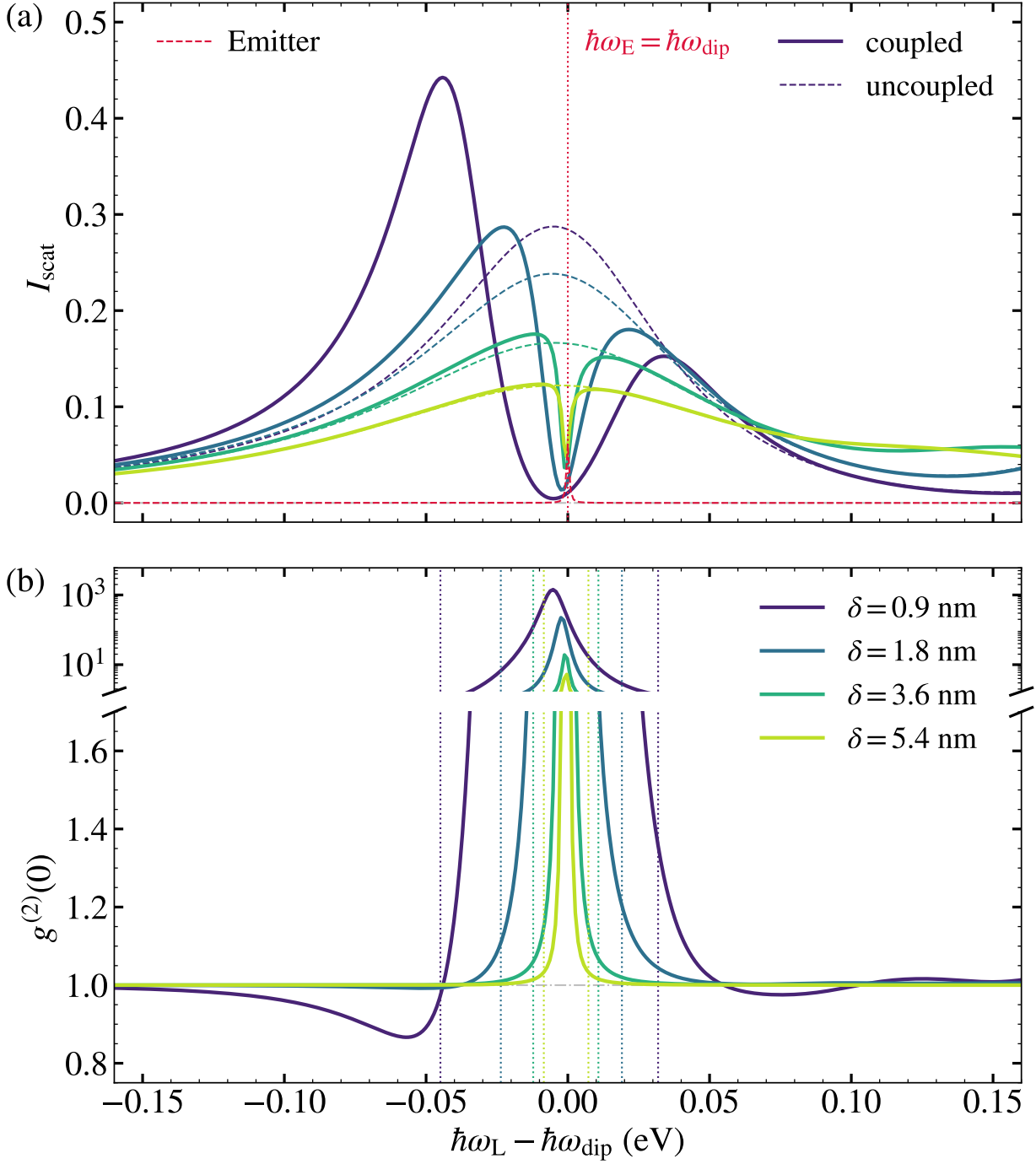
Figure 2: (a) Far-field spectra for the bare cavities in Figure 1 (dashed lines) and the hybrid SP-QE samples (solid lines) that result from introducing a vertically-oriented molecule at the gap center. I_{scat} is plotted against the detuning between the incident laser and the dipolar SP, $\hbar\omega_{\text{L}} - \hbar\omega_{\text{dip}}$, and only in the vicinity of this cavity mode. The dashed red line represents the free-standing QE spectrum, which is, in all cases, at resonance with the dipolar SP, $\omega_{\text{E}} = \omega_{\text{dip}}$ (vertical dotted line). (b) Zero-delay second-order correlation function, $g^{(2)}(0)$, versus laser detuning for the same NPoM-QE configurations in (a). Vertical dotted lines indicate the plexciton frequencies in the one-excitation manifold for each gap size.
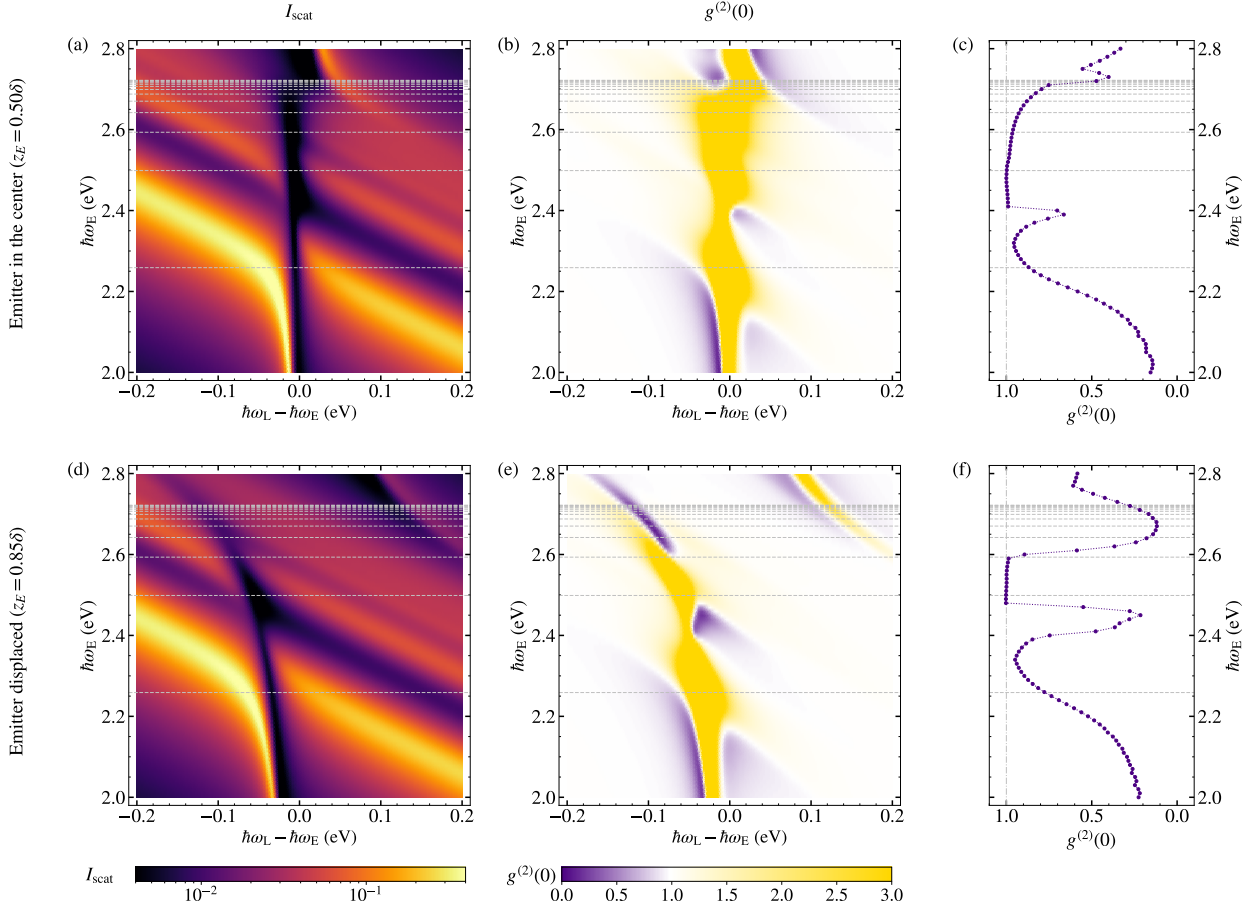
21

Figure 3: Scattering intensity I_{scat} (first column) and second-order correlation function $g^{(2)}(0)$ (second column) versus laser-QE detuning $\hbar\omega_{\text{L}} - \hbar\omega_{\text{E}}$ and QE frequency $\hbar\omega_{\text{E}}$ for emitter at the center of the gap (top, a-c) or vertically displaced (bottom, d-f). Panels in third column plot the minimum of $g^{(2)}(0)$ as a function of the emitter frequency extracted from (b) and (e). In all panels, horizontal dotted lines indicate the position of the NPoM SP frequencies.
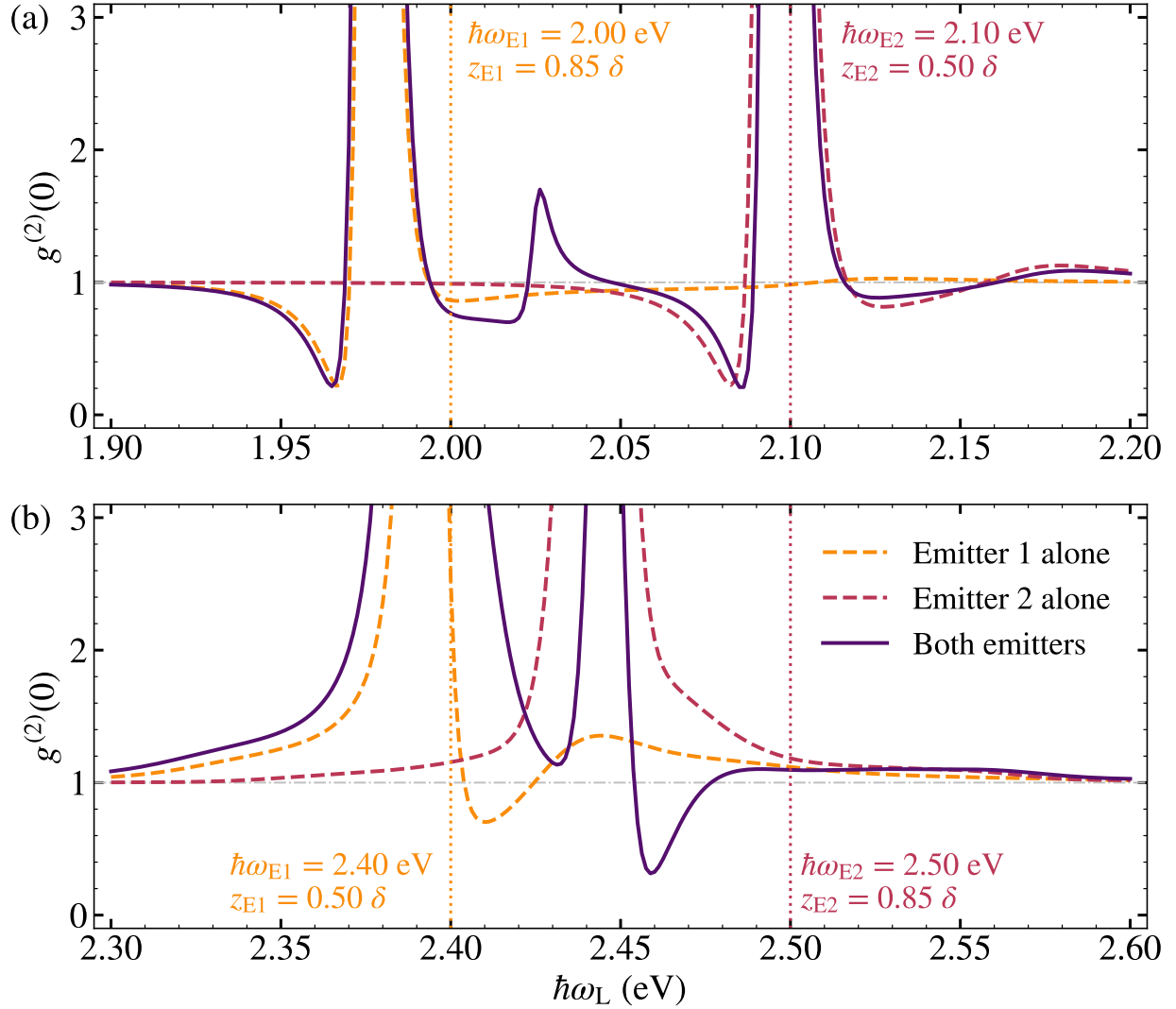
Figure 4: Second-order correlation function versus laser frequency ω_{L} for two different plexci-tonic systems, containing two QEs (one at the gap center, another vertically displaced). The QE frequencies are either red-detuned with respect to the dipolar plasmon (a) or lying within the scattering (invisibility) dip (b). Here, $g^{(2)}(0)$ for the two-emitter configurations (continuous lines) are compared against the corresponding single-emitter calculations (dashed lines). Vertical dotted lines indicate the values of $\hbar\omega_{\mathrm{E}}$ in each case.